Chemical Science

ROYAL SOCIETY OF CHEMISTRY

EDGE ARTICLE

View Article Online
View Journal | View Issue

Cite this: *Chem. Sci.*, 2025, **16**, 17408

All publication charges for this article have been paid for by the Royal Society of Chemistry

Dynamic surface radical confinement in a compact CdS–$CdIn_2S_4$ semi-coherent heterojunction for highly efficient synergetic photocatalytic selective oxidation of toluene and enhanced hydrogen production

Yuhui Liu,[ab] Xiaoxu Deng,*[b] Chuangyun Guo,[a] Shuang-Feng Yin*[cd] and Peng Chen *[a]

Received 18th June 2025
Accepted 25th August 2025

DOI: 10.1039/d5sc04474j

rsc.li/chemical-science

Efficiently activating inert C–H bonds while maintaining control over the selective pathways of complex chemical reactions involving high-energy species remains a highly challenging and as-yet unattained objective. Herein, we propose a novel concept called 'dynamic local free radical confinement-mediated mechanism' to efficiently achieve synergetic selective oxidation of toluene and hydrogen generation for the first time *via* a CdS–$CdIn_2S_4$ semi-coherent heterojunction (CCS) under two-phase conditions. Surprisingly, the optimized CCS-2 exhibited amazing catalytic efficiency and long-term stability in gram-scale experiments and automatically separated the catalyst from the product. The mechanistic study indicates that the unstable semi-coherent interface in CCS-2 establishes a channel for directed carrier migration. Furthermore, the unstable semi-coherent interface facilitates the assembly of low-coordinate cadmium sites with surface hydroxyl groups, resulting in the formation of a first-layer hydrogen bonding framework, which effectively cleaves the C–H bond and dynamically inhibits the adsorption of aldehydes, thereby inducing spatial separation between the two phases. Our study highlights a new insight into the selective regulation mediated by surface radicals and introduces a novel and universal approach for achieving environmentally friendly chemical synthesis and energy conversion.

Introduction

Precise control of target chemical reactions is crucial in chemistry.[1] Especially, selectively activating saturated benzylic C–H bonds to upgrade oxygenated products is one of the most desirable processes in the chemical and pharmaceutical industries.[2,3] Due to the high benzylic C–H bond energy and the risk of overoxidation, the traditional pathways of benzylic C–H activation require harsh reaction conditions and remain formidable challenges that have not been adequately addressed for a long time.[4,5] Photocatalytic selective oxidation of benzylic C–H bonds, facilitated by the formation of electron–hole pairs and subsequent production of active radicals, has long served as a highly effective model system for alleviating these challenging reactions under mild conditions.[6–10] Despite some progress in research on photocatalytic benzylic C–H activation, we noticed that the photogenerated holes activated the benzylic C–H bond with low oxidation kinetics, unmanageable oxidation capacity and limited substrate molecules contact area (Fig. 1a). Therefore, there are often contained O_2 reduction to generate $\cdot O_2^-$ or ·OH for participating in C–H activation, which is difficult to control the reaction course and results in a waste of electrons.

Considering the aforementioned factors, if selective oxidation of benzylic C–H bonds can be achieved while simultaneously producing clean and renewable H_2 energy, it would offer significant advantages in terms of dynamic and thermodynamic benefits as well as carrier utilization rate compared to conventional methods involving multiple steps for interconversion with electron–hole or active species.[11–15] However, the low oxidation kinetics of hole in the photocatalytic C–H bond coupling process provide dynamic advantages, enabling simultaneous hydrogen generation instead of selective C–H bond oxidation (Fig. 1a).[16] Furthermore, despite water-induced species (·OH) can activate C–H bond bonds to form oxygenated products, the high-energy species are prone to excessive

[a]*School of Chemistry and Chemical Engineering, Guizhou University, Guiyang 550025, Guizhou, China. E-mail: pchen3@gzu.edu.cn*

[b]*Key Laboratory of Electronic Composites of Guizhou Province, College of Big Data and Information Engineering, Guizhou University, Guiyang, 550025, Guizhou, China. E-mail: dxjdeng7@163.com*

[c]*College of Chemistry and Chemical Engineering, Central South University of Forestry and Technology, Changsha 410004, P. R. China. E-mail: sf_yin@hnu.edu.cn*

[d]*Advanced Catalytic Engineering Research Center of the Ministry of Education, State Key Laboratory of Chemo/Biosensing and Chemometrics, College of Chemistry and Chemical Engineering, Hunan University, Changsha 410082, P. R. China*

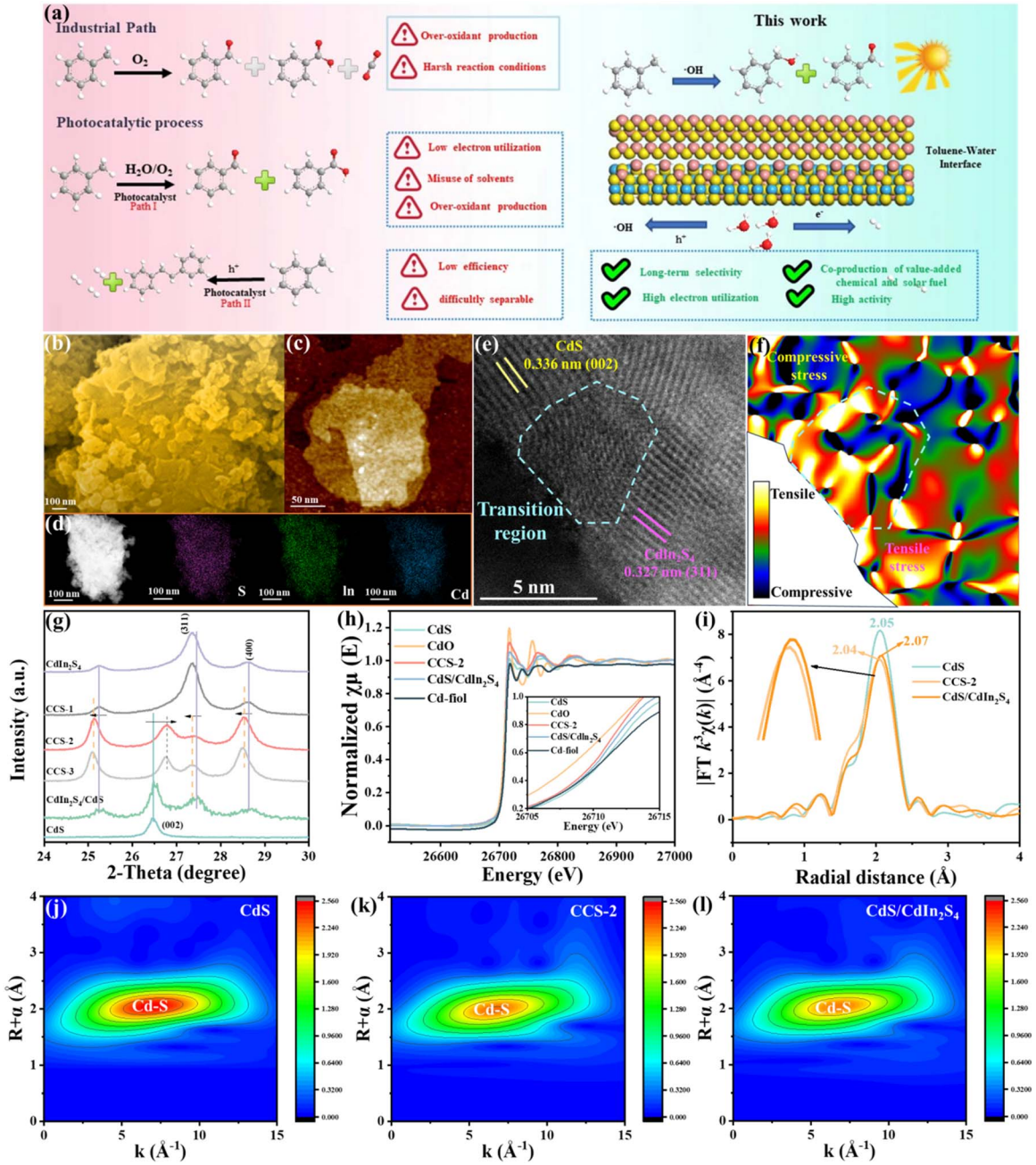

Fig. 1 (a) Strategies for the PCH reaction process of CCS. (b) SEM image, (c) AFM image, (d) element distribution diagram, (e) HAADF-STEM image, (f) GPA pattern of CCS-2. (g) The XRD patterns of samples. (h) The normalized Cd K-edge XANES spectra. (i) EXAFS R-space. Wavelet transforms of (j) CdS, (k) CCS-2 and (l) $CdS/CdIn_2S_4$.

oxidation in reactions and capturing active proton hydrogen results in the inability to generate hydrogen.[4] Moreover, due to their limited solubility in water, C–H compounds are frequently misused with inappropriate solvents, posing challenges in the separation process flow related to solvent usage. Therefore, efficiently activating inert C–H bonds while maintaining control over the selective pathways of complex chemical reactions involving high-energy species remains a highly challenging and yet unattained objective.

To address these challenges and enhance the efficiency of photocatalysis, we propose a novel concept called 'dynamic local free radical confinement mediated mechanism' for the first time. This method exploits the unstable semi-coherent interface of CdS–$CdIn_2S_4$ amphipathic heterojunction with structural disorder and a decrease in coordination number. Notably, the unstable semi-coherent interface facilitates the assembly of low-coordinate cadmium sites with surface hydroxyl groups, resulting in the formation of a first-layer hydrogen bonding framework that confines highly active radicals of ·OH and toluene and benzyl alcohol within a localized area but dynamically inhibits the adsorption of aldehydes, thereby inducing spatial separation between the two phases.

This overcomes the long-standing challenge of low selectivity for C–H activation and excessive oxidation. Moreover, the unstable semi-coherent interface in CCS-2 establishes a channel for directed carrier migration. Remarkably, the optimized CCS-2 exhibited large-scale production of H_2 and oxidized compounds while maintaining long-term selectivity retention and automatically separated the catalyst from the product (see the SI experiment section for details, Fig. S1, SI). The dynamic biphasic demonstrate practical benefits in terms of retrieving the product, expenses, efficiency, and expandability for solar hydrogen production and selective oxidation of organic compounds.

Results and discussion

Characterization of catalyst

As shown in Fig. 1b, c, S2 and S3 (SI), CCS-2 with a typical nanosheet structure, with a thickness of 4.35 nm, was created using a straightforward solvothermal approach. Furthermore, the distribution of S, In, and Cd elements within CCS-2 exhibits uniformity (Fig. 1d). The highest specific surface areas of CCS-2 were measured to be 59.5 $m^2\ g^{-1}$ (Fig. S4, SI), verifying that nanosheet structure provides more abundant active sites for PCH. According to the high-angle annular dark field scanning transmission electron microscopy (HAADF-STEM, Fig. 1e and S5, SI), the (311) plane of $CdIn_2S_4$ is represented by a lattice spacing of 0.327 nm, while the (002) plane of the hexagonal phase of CdS is represented by a lattice spacing of 0.336 nm.[17–19] Additionally, an interlaced interface between CdS and $CdIn_2S_4$ indicates the formation of intermediate coherent interfaces. Furthermore, the angle between the normal vectors of the (002) plane of CdS and (311) plane of $CdIn_2S_4$ in fast Fourier transform (FT) patterns is 14°, which is consistent with HAADF-STEM results and suggests that lattice-matching accidents are prone to occur during *in situ* hydrothermal synthesis (Fig. S6, SI).

This phenomenon can be attributed to the lattice transformation of the (311) face of $CdIn_2S_4$ into the (002) face of CdS by tensile extrusion. Moreover, the geometric phase analysis (GPA) reveals that CdS (002) experiences compression while most of the $CdIn_2S_4$ undergoes tension on CCS-2 (Fig. 1f). This has been confirmed by observing an increasing trend and a shift to higher angles in the (002) peak of CdS, while the (311) peak of $CdIn_2S_4$ demonstrates a decreasing tendency with an increase in sulfur content (Fig. 1g and S7, SI). In addition, X-ray diffraction (XRD) Rietveld refinement results show that on CCS-2, CdS is compressed while $CdIn_2S_4$ is stretched (Fig. S8 and Table S1, SI), further suggesting that CdS (002) originates from the lattice transition of stretched $CdIn_2S_4$ (311).[20] Besides, the molar ratio of the Cd/In in CCS-2 was confirmed to be 1.08 by the plasma mass spectrometry (ICP-MS) (Table S2, SI), demonstrating the unstable surfaces of CdS–$CdIn_2S_4$ heterojunction are successfully prepared. Those metastable crystal faces are prone to causing structural disorder and a decrease in coordination number, which is conducive to the enhancement of material surface activity.

Synchrotron X-ray absorption fine structure (XAFS) spectroscopy was used to further identify the structural alterations in CCS-2. As shown in Fig. 1h, S9 and Table S3 (SI), CCS-2 manifestly favors a lower energy state compared to CdS/$CdIn_2S_4$, which corresponds to an Cd oxidation state of +3.64, which is lower than that of CdS/$CdIn_2S_4$ at +3.97, suggesting that less coordination of metastable surface. In addition, electron paramagnetic resonance (EPR) analysis verified sulfur vacancies (Fig. S10, SI), demonstrating the low-coordination structure. The Fourier transform (FT) extended X-ray absorption fine structure (EXAFS) spectra, compared to CdS/$CdIn_2S_4$, show that the phase-shift corrected Cd–S bond peak is displaced from 2.07 to 2.04 Å, indicating the presence of low-coordinated Cd sites and lattice contraction in CCS-2 (Fig. 1i). As shown in Fig. 1j–l, the wavelet transform visualizes the changes occurring in the lattice of the Cd–S within the samples.

Furthermore, the material's surface electronic changes were observed *via* X-ray photoelectron spectroscopy (XPS). The S 2p pattern may be deconvoluted into two different peaks at 161.5 and 162.7 eV (Fig. S11a, SI), corresponding to S $2p_{3/2}$ and S $2p_{1/2}$ signals, corresponding the presence of S_2^{-}.[21,22] The two In 3d peaks at 444.8 and 452.4 eV correspond to In $3d_{5/2}$ and In $3d_{3/2}$ (Fig. S11b, SI), respectively, which can be attributed to typical In^{3+} in CCS-2.[23] As shown in Fig. S11c (SI), two peaks at 405.3 and 412.0 eV in the Cd 3d spectrum of CCS-2, corresponding to Cd $3d_{5/2}$ and Cd $3d_{3/2}$ signals, indicating the Cd^{2+} oxidation state of Cd, which consistent with the synchrotron radiation data.[24,25] The results indicated that the binding energy shifts of S 2p, In 3d, and Cd 3d in CCS-2 were lower than in CdS/$CdIn_2S_4$ heterojunctions, indicating a very low degree of coordination that may aid in the adsorption of the reactants.[26] In conclusion, the stretching and extrusion of the lattice lead to the formation of sub-stable transition surfaces. The defects on these surfaces eventually exhibit a low-coordination state, which enhances substrate adsorption and influences the PCH reaction.

Photocatalytic selective oxidation of toluene and hydrogen production

The main challenge in simultaneous photocatalytic selective oxidation of toluene and hydrogen production (PCH) is to control the reaction process under mild conditions. In our system, amphipathic heterojunctions were prepared and applied for PCH with a gram-level reaction without using solvent and co-catalyst. The actual reaction process can be seen in Fig. S12–S14 (SI). Obviously, the catalyst is positioned between water and toluene, enabling simultaneous contact and reaction with both substances. As shown in Fig. 2a, the lowest toluene conversion was observed over CdS (133.5 $\mu mol\ g^{-1}\ h^{-1}$, benzyl alcohol: 50.8%, benzaldehyde: 46.1%, and bibenzyl: 3.1%), $CdIn_2S_4$ (76.6 $\mu mol\ g^{-1}\ h^{-1}$, benzyl alcohol: 51.2%, benzaldehyde: 46.7%, and bibenzyl: 2.1%) and CdS/$CdIn_2S_4$ (477.8 $\mu mol\ g^{-1}\ h^{-1}$, benzyl alcohol: 52.5%, benzaldehyde: 45.2%, and bibenzyl: 2.3%). On the other hand, CCS-2 (CdS–$CdIn_2S_4$) exhibited the highest toluene conversion, benzyl alcohol, and benzaldehyde selectivity (1330.4 $\mu mol\ g^{-1}\ h^{-1}$, benzyl alcohol: 50.3%, benzaldehyde: 48.7%, and bibenzyl:

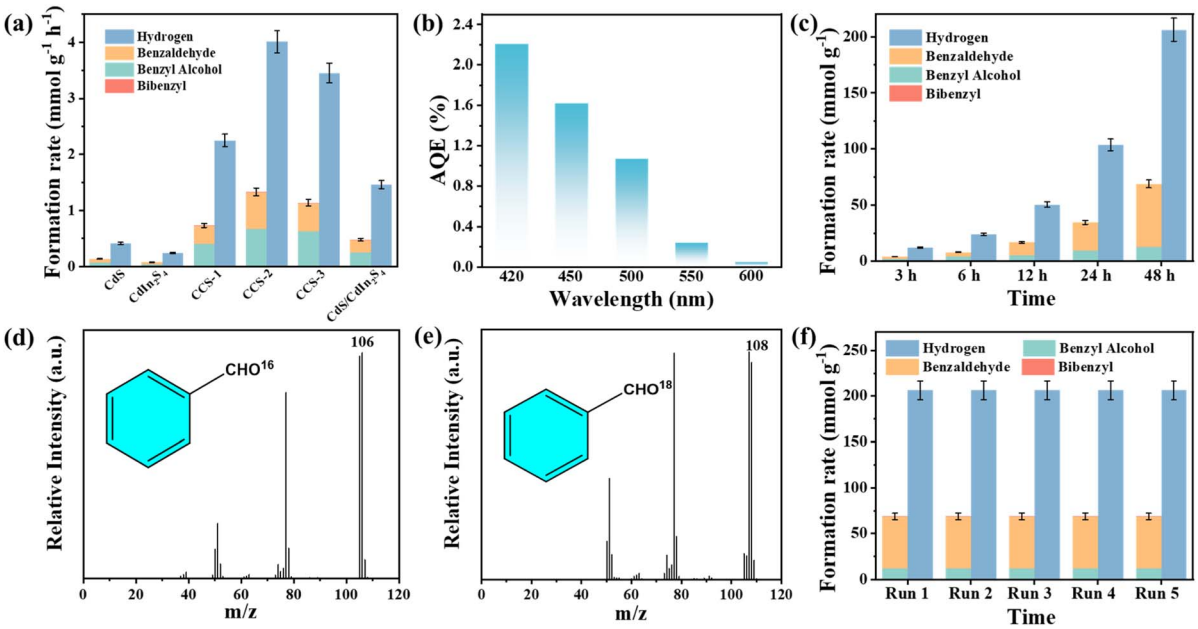

Fig. 2 (a) Time-dependent photocatalytic activities of PCH for as-prepared samples for 3 h. (b) The hydrogen production AQE for CCS-2. (c) Time-dependent toluene conversion (3 to 48 h) for CCS-2. The isotope tracing experiments of (d) $H_2{}^{16}O$ and (e) $H_2{}^{18}O$. (f) Recyclability toward PCH for 48 h for CCS-2.

1.0%). Importantly, there is no over-oxidation product of benzoic acid or CO_2 or coupling product were observed, suggesting the highly controlled oxidation of toluene process (Fig. S15, SI). In addition, the hydrogen production rate of CCS-2 is 4010.1 μmol g^{-1} h^{-1}, which is *ca.* 9.8, 16.7 and 2.7 times greater than that of the CdS (410.1 μmol g^{-1} h^{-1}), $CdIn_2S_4$ (240.0 μmol g^{-1} h^{-1}), $CdS/CdIn_2S_4$ (1460.1 μmol g^{-1} h^{-1}), respectively. The toluene conversion rate is well-matched the hydrogen production rate. Excitingly, the apparent quantum efficiency (AQE) values for the hydrogen production over CCS-2 at 420 nm is nearly 2.2% (Fig. 2b).

For the most reported works, the over-oxidation product of benzoic acid or CO_2 could be obtained by prolong reaction time.[27] Therefore, the time-dependent toluene conversion over CCS-2 sample was also tested. With the increase of irradiation time from 3 to 48 h, the toluene conversion rate increased (conversion rate: 0.08%, 0.17%, 0.36%, 0.73%, 1.46%, Fig. 2c and Table S4, SI), while benzoic acid was not detected in the product (Fig. S16, SI). Importantly, CCS-2 will sink into the water the material after operated for 48 h, indicating that the prepared catalyst can effectively suppress excessive oxidation of toluene to benzoic acid (Fig. S17, SI). Moreover, the experiment of hydrogen production from D_2O proved that the hydrogen in the reaction system came from water rather than toluene (Fig. S18, SI). In the isotope experiment using $H_2{}^{18}O$, the ^{16}O in the product was replaced by ^{18}O, which suggesting that the oxygen in the products originated from water (Fig. 2d and e). Furthermore, pH-dependent studies revealed optimal catalytic performance under neutral conditions, whereas acidic media induced catalyst deactivation and competitive hydrogen evolution, suppressing organic transformations, while alkaline conditions diminished activity due to hydroxyl-induced active-site passivation (Fig. S19).

The toluene substrates extension has been investigated to broaden the reaction applicability. The observed differences in reactivity can indeed be attributed to electronic effects, where electron-donating groups (*e.g.*, $-CH_3$ or $-C(CH_3)_3$) enhance the electron density of the aromatic ring, facilitating C–H bond activation, while electron-withdrawing groups (*e.g.*, –Cl or –Br) exhibit slightly lower reactivity due to reduced electron density. This trend aligns with our mechanistic studies, which highlight the role of surface hydroxyl groups in modulating substrate adsorption and activation (Table S5, SI). For industrial production, the recyclability and stability of the catalyst is an important role and are verified by cyclic experiments. As shown in Fig. 2f, S20 and S21 (SI), there is no obvious deactivation after five cycles of photocatalytic test, indicating that the prepared catalyst has high stability and recyclability. Above all, CCS-2 exhibited excellent photocatalytic activity, selectivity and durability, which means that the considerable prospects in photocatalytic hydrogen production synergistic with toluene oxidation. Additionally, our reaction system was implemented delicately without using solvents and co-catalyst, this implies easier separation of products and results in an efficient and economically viable reaction system, with promising industrial application prospects.

Charge transfer behavior

As the mobility of charge carriers controls the activity of toluene oxidation and hydrogen generation rate, a series of studies on electron and hole mobility is currently underway. As shown in Fig. S22 (SI), the enhanced absorption intensity and edge of CCS indicate its potential as a catalyst under visible light. Accordingly, the band gap values of CdS and $CdIn_2S_4$ are about 2.21

and 2.33 eV, respectively (Fig. S23, SI). Moreover, the conduction band (CB) position of the CdS and $CdIn_2S_4$ was measured to be −0.50 and −0.71 V (Fig. S24, SI). Consequently, the valence band (VB) potentials of CdS and $CdIn_2S_4$ are evaluated to be 1.71 and 1.62 V (*vs.* NHE) (Fig. S25, SI). Based on the above results and *in situ* XPS spectra, the electron transfer path can be described as follows: $CdIn_2S_4$ acts as an electron acceptor, while the migration of electrons occurs from CdS to $CdIn_2S_4$, suggesting the photogenerated electrons follow the S-scheme transfer mechanism (Fig. S26, SI).

While the drift trend of charge carriers is easily understood, predicting their intrinsic drift behavior remains challenging. There is reported that the (002) facet of CdS is a reductive crystal plane,[28] which originates from a lattice transition induced by tensile strain in $CdIn_2S_4$ and offers significant advantages for carrier transport in the heterojunction. To confirm the functionality of intermediate coherent interfaces, density functional theory (DFT) calculation has been carried out. As shown in Fig. S27 (SI), the differential charge density suggests that the coherent interface of CdS acts as an internal carrier convergence center, which drives the excited electrons from CdS into $CdIn_2S_4$. To further illustrate the transmission of photogenerated electrons at the interface of CCS heterojunction, light-assisted Kelvin Probe Force Microscopy (KPFM) has been carried out (Fig. 3a). The higher contact potential difference value of 4.6 mV for CCS-2, compared to 2.8 mV for CdS/$CdIn_2S_4$, underscores the enhanced charge separation efficiency facilitated by the semi-coherent interface in CCS-2. This difference arises from the unique electron screening effect at the unstable interface, which reduces carrier loss. These results collectively highlight the critical role of the semi-coherent interface in optimizing charge transfer dynamics.

Femtosecond time-resolved transient absorption (fs-TA) spectroscopy was conducted to confirm the generation and transfer mechanism of photogenerated carriers at the intermediate coherent interface (Fig. 3b–e and S28, SI). CCS-2 and CdS/$CdIn_2S_4$ exhibited a four-step electron relaxation process.[29] Since the electron diffusion lifetime on the lattice is very short (a few picoseconds) attributing τ_1 (3.23 ps) to electron leaps,[30] attributing τ_2 (50.42 ps) to sulfur defect trapping,[31] and the slower quenching process of τ_3 (1124.99 ps) describes the recombination of the electrons in the CB with the holes in the VB.[32] Therefore, attributing the new fitted lifetime of 60.13 ps (τ_4) attributed to interfacial electron transport is reasonable,[33] suggesting that additional steps are required for electron transport from CdS to $CdIn_2S_4$ at the CCS-2 interface. In addition, the interface transport time is long compared to CdS/$CdIn_2S_4$, which is notably slower than in CdS/$CdIn_2S_4$, confirming the semi-coherent interface's role as an electron trap that mitigates recombination.

By implementing a logical regulation of charge carriers, one can anticipate a remarkable trend in the migration of carriers. The charge effective mass calculations showed that CCS has the least charge effective mass, indicating the maximum charge transfer rate in the heterojunction, as shown in Fig. S29 (SI). Furthermore, CCS-2 exhibited weakest photoluminescence (PL) intensity and the longest charge average lifetimes (Fig. 3f and g), confirming the highest carrier separation efficiency in the

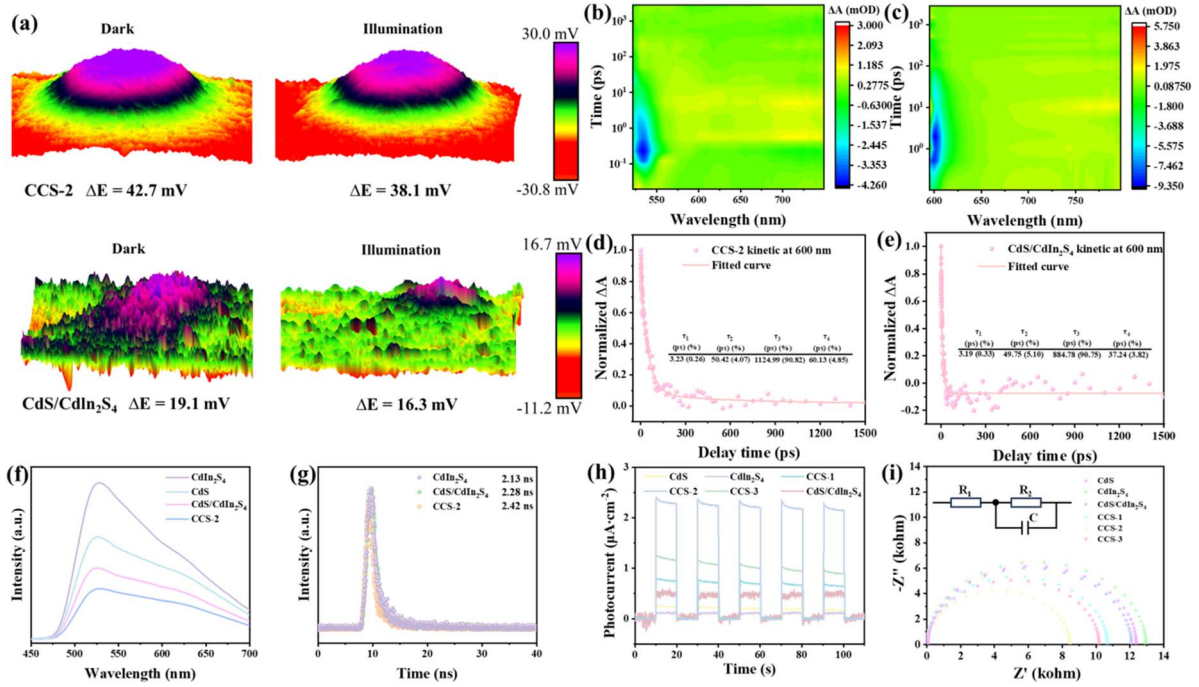

Fig. 3 (a) KPFM images of CCS-2 and CdS/$CdIn_2S_4$ in the dark and under irradiation and the corresponding contact potential differences. Pseudocolor fs-TA spectra of (b) CCS-2 and (c) CdS/$CdIn_2S_4$. The typical TA kinetics probed at 600 nm for (d) CCS-2 and (e) CdS/$CdIn_2S_4$. (f) The photoluminescence (PL) spectra of samples. (g) Time-resolved fluorescence spectra of samples. (h) Photocurrent of samples. (i) Electrochemical impedance of samples.

heterojunctions. Additional evidence demonstrates that CCS-2 has the largest photocurrent density and the smallest electrochemical impedance (Fig. 3h and i), indicating a significant enhancement of photogenerated charge separation at the CCS, thereby leading to heightened photocatalytic activity. In summary, the coherent interface of CdS serves as an internal carrier convergence center. This facilitates the formation of the built-in electric field, leading to the directional combination of charges instead of random recombination at the heterojunction interfaces.

Catalytic mechanism

The generation of hydrogen from electron-proton interaction in hydrogen atoms is undeniable; However, the active species and reaction process involved in the oxidation of toluene are still unidentified. Firstly, we carried out *in situ* Fourier transform infrared (FTIR) spectroscopy analysis to examine the detailed reaction process on CCS under illumination. The *in situ* FTIR spectra of 2936.4, 3460, 1751.7, 1507.3, 1442.2, and 1347.6 cm^{-1} belongs to the typical absorption peak of toluene, water, benzaldehyde, aromatic ring, and benzyl alcohol, respectively (Fig. 4a).[34–37] Notably, no characteristic peaks of benzoic acid and CO_2 were detected. Hence, the oxidation of toluene results in the formation of benzyl alcohol and benzaldehyde as intermediate products. Second, the oxidation active species is confirmed by the free radical capture experiment. As illustrate in Fig. S30 and S31 (SI), a significant reduction in ·OH radicals and h^+ capture agents, indicating ·OH radicals know, the formation of ·OH radicals are a huge obstacle for $CdIn_2S_4$ and CdS. However, compared to free ·OH groups [$\phi_{(\cdot OH(free)/\cdot OH(free))} \approx 2.3$–$2.4$ V], surface-adsorbed ·OH groups could be oxidized to surface ·OH radicals at less of a redox potential [$\phi_{(\cdot OH(ads)/\cdot OH(ads))} \approx 1.5$ V].[34,38] Based on the combination of EPR results, we hypothesize that the adsorbed ·OH groups on the surface of CCS-2 can undergo a reaction with photogenerated holes, resulting in the generation of ·OH active species (Fig. S32, SI). To further understand the adsorption of surface ·OH, we performed XPS analysis. As shown in Fig. S33 (SI), the 531.7 eV component belongs to the surface ·OH group.[39,40] Moreover, the surface-adsorbed ·OH concentration was quantitatively experimented using the F-substitution method.[41] As shown in Fig. S34 (SI), CCS-2 exhibited 4.9 times more $CdIn_2S_4$,

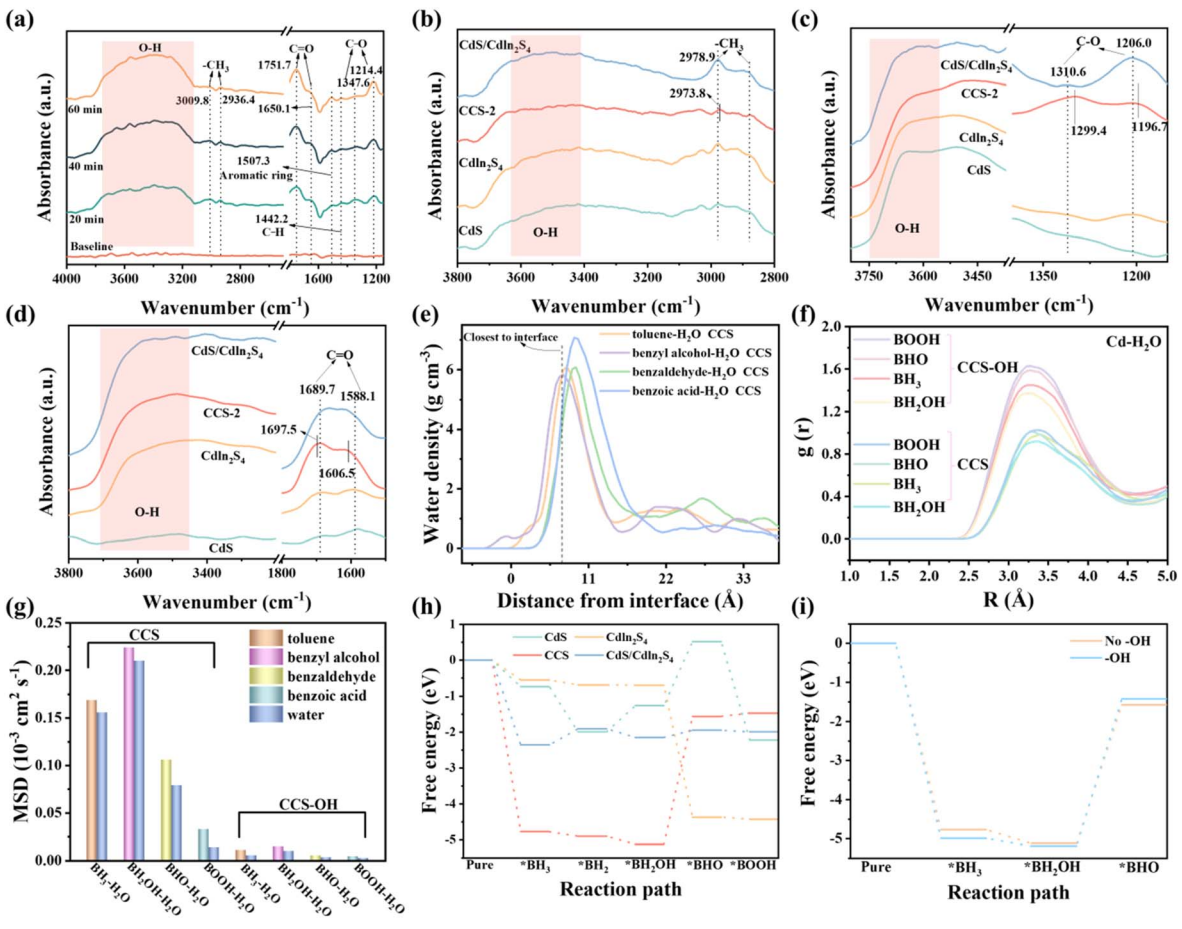

Fig. 4 (a) *In situ* FTIR of CCS-2 under reaction condition. *In situ* FTIR spectra of (b) toluene–water, (c) benzyl alcohol–water, and (d) benzaldehyde–water adsorbed on samples. (e) The density distribution curve of water in each system. (f) The radial distribution function of Cd active site with water on CCS and CCS-OH. (g) The diffusion coefficients of organic matter and water on CCS and CCS-OH. (h) The adsorption Gibbs free energy in the oxidation of toluene for CdS, $CdIn_2S_4$, CCS and CdS/$CdIn_2S_4$. (i) The adsorption Gibbs free energy with CCS-OH compare to CCS.

suggesting the surface of the CCS-2 has a high surface hydroxyl coverage.

In our system, the key is to control the simultaneous oxidation of hydrogen and toluene while maintaining the selectivity of toluene oxidation. Fig. S35 (SI) illustrates that CCS-2 exhibits a low contact angle and similar affinity for water and toluene, indicating its potential as a Pickering emulsion catalyst for simultaneous oxidation of toluene and hydrogen production through regulated catalytic reactions within distinct interfacial environments.[42] However, the catalyst has a smaller contact angle with the toluene–benzyl alcohol solution compared to toluene and water, but a larger contact angle with the toluene–benzyl alcohol-benzaldehyde solution, suggesting CCS-2 is able to suppress the oxidation of toluene to benzoic acid or CO_2 (Fig. S36, SI). Therefore, it can be concluded that CCS-2 exhibits unique surface properties at the interfaces of two liquid media, enabling simultaneous activation of toluene and intermediates as well as water.

To further understand the unique two-phase interface relationship, *in situ* FTIR measurements using various toluene-based substances and water were conducted. As shown in Fig. 4b, compared with CdS, $CdIn_2S_4$, and CdS/$CdIn_2S_4$, the characteristic ν(C–H) band of toluene of CCS-2 has a red shift in the concomitant toluene and water, indicating that CCS-2 has a preference for adsorbing toluene.[43,44] Furthermore, the characteristic ν(C–O) band of benzyl alcohol also exhibited a red shift on CCS-2 in the concomitant benzyl alcohol and water (Fig. 4c), while benzaldehyde (Fig. 4d), benzoic acid (Fig. S37, SI) and 1,2-diphenylethane (Fig. S38, SI) adsorption exhibited a blue shift,[45,46] suggesting the CCS-2 support the existence of benzyl alcohol and detest benzaldehyde, benzoic acid and 1,2-diphenylethane in a two-phase aqueous solution. In addition, fitting the broad peaks of H_2O in the *in situ* FTIR spectra yielded a ratio of the linear structure (DA) to the hydrogen-bonding network (DDAA) of CCS-2 of 2.01, which is higher than that of CdS (1.48), $CdIn_2S_4$ (1.38), and CdS/$CdIn_2S_4$ (1.69) (Fig. S39, SI).[47] The DA structure facilitates water adsorption on the surface of the material and further formation of surface hydroxyl groups.

In order to analyze the effect of surface hydroxyl groups on the reaction kinetics, the density distributions, free diffusion coefficients and coordination numbers of CCS (without surface hydroxyl groups) and CCS-OH (with surface hydroxyl groups) were simulated using density distribution curves, the radial distribution function (RDF) and the mean square displacement (MSD) method. Firstly, the theoretical models of CCS-OH and CCS are analyzed, and it is found that organic matter and water on CCS-OH are closer to the interface (Fig. S40 and S41, SI). Second, in the benzyl alcohol–water system, water is closer to the interface than in the other systems, corresponding to the contact angle results (Fig. 4e). As shown in Fig. S42 and S43 (SI), the distances of both organic matter and water from the active site Cd are shorter in CCS-OH than on CCS. In addition, the RDFs of organic matter and water with the active site Cd in CCS-OH and CCS were compared and the coordination number was calculated. The high peak value and coordination number of CCS-OH structure indicate that the surface hydroxyl group promotes the adsorption of H_2O on the catalyst, which is conducive to the formation of hydroxyl radical (Fig. 4f and Table S6, SI). Interestingly, the coordination number of cadmium active sites on CCS-OH with toluene and benzyl alcohol is higher than that of CCS, while the opposite is true with benzaldehyde and benzoic acid, suggesting that the adsorption of organic substances by surface hydroxyl groups is selective (Fig. S44 and Table S7, SI). Finally, MSD analysis showed that the surface hydroxyl group reduced the diffusion coefficient, again proving that the surface ·OH was beneficial to the adsorption of organic matter and water (Fig. 4g).

The Gibbs free energy have been computed in order to better understand the internal reaction process. Remarkably, the ΔG_{H^*} for CCS is significantly smaller (−0.29 eV) than that of CdS/$CdIn_2S_4$ (−0.13 eV), CdS (−0.08 eV) and $CdIn_2S_4$ (−0.04 eV), suggesting that CCS demonstrates superior activity as an HER catalyst compared to other materials (Fig. S45, SI). On the other hand, compare to CdS, $CdIn_2S_4$, and CdS/$CdIn_2S_4$, CCS exhibit the lowest free energies in the toluene oxidation (Fig. 4h, S46 and S47, SI). Notably, the reaction from toluene to benzyl alcohol becomes increasingly exergonic, while the reactions from benzyl alcohol to benzaldehyde and then to benzoic acid become increasingly endergonic, suggesting CCS can fundamentally control their selectivity. Furthermore, the adsorption energy of the toluene coupling process is notably positive than that of the oxidation process (Fig. S48, SI), suggesting the competitive oxidation process of toluene yields benzyl alcohol and benzaldehyde as the primary products. To further confirm the impact of surface hydroxyl groups, DFT calculations are being carried out (Fig. S49, SI). As shown in Fig. S50 (SI), CCS exhibit the related adsorption energies for toluene (−4.77 eV) and H_2O (−4.69 eV), indicating even under initial conditions (without hydroxyl radicals), the catalyst could theoretically react with water and toluene at the same time (consistent with contact angle results). Notably, the adsorption energy for benzyl alcohol is −5.12 eV, while benzaldehyde, benzoic acid, and 1,2-diphenylethane are −1.57, −1.47 and −1.16 eV, demonstrating stronger adsorption of benzyl alcohol than others. It is noteworthy that the adsorption energies of toluene and benzyl alcohol are more negative and the adsorption energy of benzaldehyde is more positive in the paths with surface hydroxyl groups (Fig. 4i). Therefore, the low-coordinate CdS–$CdIn_2S_4$ heterojunction assembles hydroxyl groups to dynamically regulate substrate adsorption, enhancing both the selectivity of toluene oxidation and the rate of hydrogen production.

Consequently, the final path for toluene oxidation is obtained (Fig. S51, SI). The catalyst initially adsorbs both water and toluene during the reaction. With the formation of surface hydroxyl groups, the catalyst enhances the adsorption of toluene and oxidizes it to benzyl alcohol, with the concomitant production of hydrogen. Benzyl alcohol is more susceptible to the surface hydroxyl groups of the catalyst, and its adsorption capacity to the toluene–benzyl alcohol solution increases, leading to a gradual transfer of the catalyst to the toluene solution, which in turn oxidizes benzyl alcohol to benzaldehyde. However, when benzaldehyde is present in the toluene–benzyl alcohol solution, the catalyst repels benzaldehyde, leading to a gradual transfer of the catalyst to water again, at which point

further oxidation of benzaldehyde to benzoic acid is no longer possible, and ultimately, the selectivity of benzyl alcohol and benzaldehyde is greatly improved. Most importantly, we explored a way for surface hydroxyl groups to modulate interfacial adsorption, which is conducive to improving the selectivity of organic oxidation.

Conclusions

In conclusion, we report a novel concept of dynamic local free radical confinement-mediated mechanism to achieve photocatalytic selective oxidation of C–H bonds and H_2 generation for the first time *via* a CdS–$CdIn_2S_4$ heterojunction with a stable semi-coherent interface. Strikingly, the optimized heterojunction displayed excellent photocatalytic activity and long-term stability, and underwent spontaneous phase separation from aqueous solutions. Different from the previously reported mechanism, our work reveals that the low-coordinate CdS–$CdIn_2S_4$ heterojunction assembles hydroxyl groups to dynamically regulate substrate adsorption, enhancing both the selectivity of toluene oxidation and the rate of hydrogen production. Additionally, the unstable semi-coherent interface acts as an active site for the fast and continual consumption of photogenerated electrons, encouraging the separation of electron–hole pairs. Our work presents a new horizon for C–H bond activation and offers instructive guidance on rationally constructing photocatalytic systems in terms of product retrieval, cost-effectiveness, efficiency, and scalability for solar hydrogen production and the selective oxidation of organic compounds.

Experimental section

Synthesis of $CdIn_2S_4$

2 mmol of $InCl_3 \cdot 4H_2O$, 1 mmol of $Cd(NO_3)_2 \cdot 4H_2O$ and 4 mmol of TAA were melted in 160 mL deionized water. The concoction was heated to 90 °C and stirred violently for 5 h. After cooling the mixture to 25 °C, ultrasonic treatment for 1 h. Then washed with deionized water and anhydrous ethanol several times. After centrifugation, $CdIn_2S_4$ was obtained by grinding after 80 °C overnight.

Synthesis of CdS

The synthesis process is similar to $CdIn_2S_4$. The difference is that no $InCl_3 \cdot 4H_2O$ is added, and the amount of $Cd(NO_3)_2 \cdot 4H_2O$ and TAA are 2 mmol, respectively.

Synthesis of CCS-*X* (1–3)

The synthesis process is similar to $CdIn_2S_4$. The difference is that the amounts of $Cd(NO_3)_2 \cdot 4H_2O$ and TAA for CCS-1, CCS-2 and CCS-3 were 2.5 and 4.5 mmol, 3 and 5 mmol, and 4 and 6 mmol, respectively.

Synthesis of CdS/$CdIn_2S_4$

Disperse 0.5 mmol CdS and 0.5 mmol $CdIn_2S_4$ into 40 mL *N*,*N*-dimethylformamide (DMF) and stir for 0.5 h. Then ultrasonic treatment for 3 h. After washing with deionized water and ethanol, the final products were centrifuged and dried for 12 h in an oven at 80 °C.

Photocatalytic activity evaluation

The photocatalytic research projects were conducted in a closed reactor equipped with a compressing reflux device. Initially, 10 mL of deionized water and 10 mL of toluene were used to distribute 20 mg of catalyst. After a vacuum pump drained the gas in the reaction system, a 300 W Xe lamp was used to initiate the reaction. Following a specified irradiation time, a gas chromatography apparatus (GC9790 plus, Fuli instruments) was used to quantify the gaseous products. The liquid products were evaluated subjectively and quantitatively using ^{1}H NMR and gas chromatography (Shimadzu GC 2014 Plus).

Author contributions

Yuhui Liu (data curation: lead; formal analysis: lead; investigation: lead; writing – original draft: lead; software: lead); Xiaoxu Deng (conceptualization: lead; data curation: lead; formal analysis: lead; funding acquisition: lead; supervision: lead; writing – review & editing: lead); Chuangyun Guo (methodology: lead); Shuang-Feng Yin (formal analysis: lead; resources: equal); Peng Chen (data curation: lead; project administration: lead; supervision: lead).

Conflicts of interest

There are no conflicts to declare.

Data availability

Supplementary information: The data supporting this article have been included as part of the SI. See DOI: **https://doi.org/10.1039/d5sc04474j**.

Acknowledgements

This project was financially supported by National Natural Science Foundation of China (No. 22268015), Key Laboratory of Carbon-based Energy Molecular Chemical Utilization Technology in Guizhou Province (No. 2023008). The authors would like to thank Scientific Compass (**https://www.shiyanjia.com**) for materials characterizations, and thanks for the computing support of the State Key Laboratory of Public Big Data, Guizhou University.

References

1 C. Zhang, E. Kazuma and Y. Kim, *J. Am. Chem. Soc.*, 2022, **144**, 10282–10290.
2 S. K. Sinha, P. Ghosh, S. Jain, S. Maiti, S. A. Al-Thabati, A. A. Alshehri, M. Mokhtar and D. Maiti, *Chem. Soc. Rev.*, 2023, **52**, 7461–7503.
3 T. Shen, Y. L. Li, K. Y. Ye and T. H. Lambert, *Nature*, 2023, **614**, 275–280.

4 P. F. Han, X. Mao, Y. C. Jin, S. Sarina, J. F. Jia, E. R. Waclawik, A. J. Du, S. E. Bottle, J. C. Zhao and H. Y. Zhu, *Angew. Chem., Int. Ed.*, 2023, **62**, e202215201.
5 L. Zhang and T. Ritter, *J. Am. Chem. Soc.*, 2022, **144**, 2399–2414.
6 M. Y. Gao, H. Bai, X. F. Cui, S. Y. Liu, S. Ling, T. T. Kong, B. Bai, C. Y. Hu, Y. T. Dai, Y. G. Zhao, L. Zhang, J. Zhang and Y. J. Xiong, *Angew. Chem., Int. Ed.*, 2022, **61**, e202215540.
7 T. Schmidt-Räntsch, H. Verplancke, J. N. Lienert, S. Demeshko, M. Otte, G. P. Van Trieste, K. A. Reid, J. H. Reibenspies, D. C. Powers, M. C. Holthausen and S. Schneider, *Angew. Chem., Int. Ed.*, 2022, **61**, e202115626.
8 N. Luo, W. Nie, J. Mu, S. Liu, M. Li, J. Zhang, Z. Gao, F. Fan and F. Wang, *ACS Catal.*, 2022, **12**, 6375–6384.
9 H. Wang, X. Li, X. Zhao, C. Li, X. Song, P. Zhang, P. Huo and X. Li, *Chin. J. Catal.*, 2022, **43**, 178–214.
10 Y. J. Wang, X. Li, Y. K. Chen, Y. Li, Z. Liu, C. Q. Fang, T. Wu, H. S. Niu, Y. Li, W. G. Sun, W. J. Tang, W. Xia, K. P. Song, H. Liu and W. J. Zhou, *Adv. Mater.*, 2023, **35**, 2305257.
11 T. von Muenchow, S. Dana, Y. Xu, B. B. Yuan and L. Ackermann, *Science*, 2023, **379**, 1036–1042.
12 B. G. Wu, L. P. Zhang, B. J. Jiang, Q. Li, C. G. Tian, Y. Xie, W. Z. Li and H. G. Fu, *Angew. Chem., Int. Ed.*, 2021, **60**, 4815–4822.
13 M. Y. Qi, Y. H. Li, M. Anpo, Z. R. Tang and Y. J. Xu, *ACS Catal.*, 2020, **10**, 14327–14335.
14 J. C. Zhang and M. Rueping, *Chem. Soc. Rev.*, 2023, **52**, 4099–4120.
15 M. Y. Qi, M. Conte, M. Anpo, Z. R. Tang and Y. J. Xu, *Chem. Rev.*, 2021, **121**, 13051–13085.
16 Y. Miao, Z. Li, L. Luo, W. Chen, L. Ma, K. Fan, Y. Song, Y. Hu, R. Li and M. Shao, *Appl. Catal., B*, 2025, **361**, 124588.
17 Q. M. Sun, N. Wang, J. H. Yu and J. C. Yu, *Adv. Mater.*, 2018, **30**, 1804368.
18 Y. X. Tan, Z. M. Chai, B. H. Wang, S. Tian, X. X. Deng, Z. J. Bai, L. Chen, S. Shen, J. K. Guo, M. Q. Cai, C. T. Au and S. F. Yin, *ACS Catal.*, 2021, **11**, 2492–2503.
19 C. Zhu, C. A. Liu, Y. J. Fu, J. Gao, H. Huang, Y. Liu and Z. H. Kang, *Appl. Catal., B*, 2019, **242**, 178–185.
20 Y. Chen, D. L. Lu, L. A. Kong, Q. Y. Tao, L. K. Ma, L. T. Liu, Z. Y. Lu, Z. W. Li, R. X. Wu, X. D. Duan, L. Liao and Y. Liu, *ACS Nano*, 2023, **17**, 14954–14962.
21 Y. Liu, Y. Wu, Y. Liu, Y. Wang, X. Sun, P. Chen and S.-F. Yin, *ACS Catal.*, 2024, **14**, 7726–7735.
22 H. Wang, Y. Xia, H. Li, X. Wang, Y. Yu, X. Jiao and D. Chen, *Nat. Commun.*, 2020, **11**, 3078.
23 H. J. Zhang, Y. J. Gao, S. G. Meng, Z. R. Wang, P. X. Wang, Z. L. Wang, C. W. Qiu, S. F. Chen, B. Weng and Y. M. Zheng, *Adv. Sci.*, 2024, **11**, 2400099.
24 S. Xu, Q. Gao, Z. Y. Hu, Y. T. Lu, Y. L. Qin and Y. L. Li, *ACS Catal.*, 2023, **13**, 13941–13954.
25 S. Chattopadhyay, A. B. Naden, W. S. J. Skinner, G. Kerherve, D. J. Payne and J. T. S. Irvine, *Adv. Energy Mater.*, 2023, **13**, 2301381.
26 J. P. Jiao, X. C. Kang, J. H. Yang, S. Q. Jia, Y. G. Peng, S. Q. Liu, C. J. Chen, X. Q. Xing, M. Y. He, H. H. Wu and B. X. Han, *J. Am. Chem. Soc.*, 2024, **146**, 15917–15925.
27 X. Cao, Z. Chen, R. Lin, W.-C. Cheong, S. Liu, J. Zhang, Q. Peng, C. Chen, T. Han, X. Tong, Y. Wang, R. Shen, W. Zhu, D. Wang and Y. Li, *Nat. Catal.*, 2018, **1**, 704–710.
28 J. Wang, Y. Q. Zhang, S. J. Jiang, C. Z. Sun and S. Q. Song, *Angew. Chem., Int. Ed.*, 2023, **62**, e202307808.
29 X. W. Shi, M. Fujitsuka, Z. Z. Lou, P. Zhang and T. Majima, *J. Mater. Chem. A*, 2017, **5**, 9671–9681.
30 P. Galar, P. Piatkowski, T. T. Ngo, M. Gutiérrez, I. Mora-Seró and A. Douhal, *Nano Energy*, 2018, **49**, 471–480.
31 B. C. Qiu, L. J. Cai, N. Zhang, X. M. Tao and Y. Chai, *Adv. Sci.*, 2020, **7**, 1903568.
32 J. J. Zhang, G. Y. Yang, B. W. He, B. Cheng, Y. J. Li, G. J. Liang and L. X. Wang, *Chin. J. Catal.*, 2022, **43**, 2530–2538.
33 C. Cheng, J. J. Zhang, B. C. Zhu, G. J. Liang, L. Y. Zhang and J. G. Yu, *Angew. Chem., Int. Ed.*, 2023, **62**, e202218688.
34 L. Monico, A. Chieli, S. De Meyer, M. Cotte, W. de Nolf, G. Falkenberg, K. Janssens, A. Romani and C. Miliani, *Chem.–Eur. J.*, 2018, **24**, 11584–11593.
35 L. V. Trandafilovic, D. J. Jovanovic, X. Zhang, S. Ptasinska and M. D. Dramicanin, *Appl. Catal., B*, 2017, **203**, 740–752.
36 B. Jiang, K. Xu, J. Li, H. Lu, X. Fei, X. Yao, S. Yao and Z. Wu, *J. Hazard. Mater.*, 2021, **405**, 124203.
37 K. Lau, F. Niemann, K. Abdiaziz, M. Heidelmann, Y. K. Yang, Y. J. Tong, M. Fechtelkord, T. C. Schmidt, A. Schnegg, R. K. Campen, B. X. Peng, M. Muhler, S. Reichenberger and S. Barcikowski, *Angew. Chem., Int. Ed.*, 2023, **62**, e202213968.
38 Z. J. Li, J. J. Wang, X. B. Li, X. B. Fan, Q. Y. Meng, K. Feng, B. Chen, C. H. Tung and L. Z. Wu, *Adv. Mater.*, 2013, **25**, 6613–6618.
39 D. S. Zhang, P. J. Ren, W. W. Liu, Y. R. Li, S. Salli, F. Y. Han, W. Qiao, Y. Liu, Y. Z. Fan, Y. Cui, Y. B. Shen, E. Richards, X. D. Wen, M. H. Rummeli, Y. W. Li, F. Besenbacher, H. Niemantsverdriet, T. B. Lim and R. Su, *Angew. Chem., Int. Ed.*, 2022, **61**, e202204256.
40 R. K. Zhang, L. Lin, D. Q. Wang, Y. J. Liu, Y. J. Ling, S. Q. Zhao, R. T. Mu and Q. Fu, *ACS Catal.*, 2022, **12**, 11918–11926.
41 K. Li, H. B. Zou, X. L. Tong and H. Q. Yang, *J. Am. Chem. Soc.*, 2024, **146**, 17054–17065.
42 K. Li, H. Zou, X. Tong and H. Yang, *J. Am. Chem. Soc.*, 2024, **146**, 17054–17065.
43 N. B. Lin, F. Hu, Y. L. Sun, C. X. Wu, H. Y. Xu and X. Y. Liu, *Adv. Funct. Mater.*, 2014, **24**, 5284–5290.
44 Z. J. Bai, S. Tian, T. Q. Zeng, L. Chen, B. H. Wang, B. Hu, X. Wang, W. Zhou, J. B. Pan, S. Shen, J. K. Guo, T. L. Xie, Y. J. Li, C. T. Au and S. F. Yin, *ACS Catal.*, 2022, **12**, 15157–15167.
45 J. Liu, P. Wang, W. Qu, H. Li, L. Shi and D. Zhang, *Appl. Catal., B*, 2019, **257**, 117880.
46 J. Yu, X. Wang, L. Chen, G. Lu, G. Shi, X. Xie, Y. Wang and J. Sun, *Chem. Eng. J.*, 2022, **435**, 135033.
47 R. Verduci, F. Creazzo, F. Tavella, S. Abate, C. Ampelli, S. Luber, S. Perathoner, G. Cassone, G. Centi and G. D'Angelo, *J. Am. Chem. Soc.*, 2024, **146**, 18061–18073.